Achromatic Needle Focusing with Superresolution Enabled by a Ring-Shaped Acoustic Metalens

Lijuan Fan and Jun Mei [*]

School of Physics, South China University of Technology, Guangzhou 510640, China

Superresolution metalenses that can realize a far-field needle focusing effect are highly desired in various applications, such as medical diagnosing, ultrasonic detection, and underwater communication. Here, we propose a design paradigm of a metalens with superresolution for waterborne sound, which is based on metagrating and has a compact and simple configuration. The central region of the metalens is open, surrounded by a metagrating-based peripheral region. In the radial cross section, each meta-atom contains two elliptical iron cylinders that are intelligently designed to deflect the impinging wave along the desired direction towards the intended focal spot. In this way, a needle focusing effect with high intensity and superresolution is achieved in the far-field region, where the conventional Rayleigh-Abbe diffraction limit is broken due to the coherent interference of the ± 1 order diffraction channels. Since the design principle does not rely on sharp resonances, the foci of waves carrying different frequencies partially overlap so that an achromatic focusing functionality is realized where incident waves in a continuous frequency range can be simultaneously focused around the same spots. The compact, planar, and center-open configuration of the metalens not only provides a flexible and practical solution to acoustic needle focusing functionality, but also has potential applications as a powerful planar component that can be easily integrated.

I. INTRODUCTION

Relying on a gradually accumulating phase change along the wave's propagation path, conventional focusing lenses are usually bulky and costly. They have two significant features that are originated from the underlying physical mechanism. The first one is the chromatic dispersion, which implies their incapability of simultaneously focusing the incident waves with different frequencies, or leads to different focal positions at different frequencies. The second one is the finite resolution, which is limited by the Rayleigh-Abbe diffraction limit of $0.5\lambda/\text{NA}$, where λ and NA are the wavelength and numerical aperture, respectively.

Recently, metalenses have emerged as a compact platform for wave-front tailoring and focusing, with the reflected or transmitted phase precisely controlled by intendedly designed meta-atoms [1,2]. Their flat configuration or miniaturized thickness provides a compact and efficient solution to various wave-manipulating functionalities. Metalens can be designed on the basis of metasurfaces or metagratings, where both electromagnetic and acoustic metalenses were studied to demonstrate their intriguing focusing capabilities. For the electromagnetic waves, superoscillating metalens were designed to

exhibit the far-field subdiffraction focusing effect, with corresponding focal spots smaller than the Rayleigh-Abbe diffraction limit [3–6]. In addition, superoscillatory lenses with an enlarged depth of focus were fabricated to generate subdiffraction-limit light sheets with reduced beam divergence [7–11].

In parallel, pioneering works were done with regard to acoustic metalenses. Researchers demonstrated the acoustic needle focusing effect using different methods, such as fabricating a miniature transducer with the press-focusing technique [12], designing an active and configurable planar metasurface with piezoelectric transducers [13], using binary reflected phases on a planar surface [14], implementing LiNbO_3 ultrahigh frequency transducers as a microbeam acoustic tweezer [15], projecting different spatial frequency components to generate superoscillation packets [16], generating two symmetrical parabolic accelerating beams along the designed trajectories [17], using the double-parabolic-reflector wave-guided high-power ultrasonic transducer [18], constructing a compact and passive ultrasound metasurface at megahertz frequencies [19], using a planar ultrasonic transducer based on a metasurface piezoelectric ring array [20], utilizing an optically transparent microfiber ultrasound sensor [21]. While most acoustic metalenses are constructed from metasurfaces, few designs are developed on metagratings. Differing form measurfaces, metagratings are based on the grating diffraction theory [22,23] rather than the generalized

---

[*]phjunmei@scut.edu.cn

Snell's law (GSL) [24–37], and thus can redirect the incident wave energy along the specific direction with unitary efficiency even in the limit of extreme wave-front manipulation. In contrast, the overall efficiency of gradient metasurfaces to reroute the impinging waves along large steering angles are comparably low due to the mismatched impedances between the incident and scattered wave beams. Furthermore, the unit cells of metagratings do not need to discretize a fast-varying continuous impedance or phase profile, which substantially reduces the fabrication and testing costs. Recently, there is a growing interest on the study of metagratings for various wave-manipulation functionalities, such as anomalous reflection or refraction [22,38–43], cloaking [44], sound vortices [45], nonreciprocal transmission [46], multifunctional device [47], elastic wave manipulation [48,49], and far-field focusing [50–56].

Inspired by the above works, in this paper we propose a metagrating-based metalens to achieve a far-field, high-intensity, subdiffraction, and achromatic needle focusing effect for waterborne sounds. The reason that we choose metagrating as the platform to design the metalens is as follows. Firstly, metagrating can retain very high diffraction efficiency even for very large steering angles, which is helpful to realize an enlarged depth of focus and beneficial to achieve high-intensity subdiffraction focusing in both near-field and far-field regions. Secondly, we can independently manipulate the diffraction direction of each meta-atom in the metagrating, so that it is straightforward to obtain a needle focusing pattern by redirecting the scattered waves from different meta-atoms towards different focal spots. Thirdly, since no sharp resonance is utilized, in principle the metalens can work for different frequencies. By utilizing the above characteristics of metagrating, we design the metalens to achieve a needle focusing pattern with a large depth of focus. Interestingly, since the foci of different frequencies partially overlap with each other, we can achieve the achromatic focusing functionality where incident waves of different frequencies are simultaneously focused at the same spots. Last but not least, the metalens has a compact and planar configuration, which is easy to be integrated with other acoustic devices to implement more comprehensive and complex wave-manipulation functionalities. Therefore, we expect the proposed metalens can find applications in various scenarios, such as medical diagnosing and treating, ultrasonic detection and navigation, and underwater communication.

II. DESIGN METHOD

The metalens is axisymmetric and based on metagrating, and we start with the two-dimensional (2D) cross section of the three-dimensional (3D) metalens, as shown schematically in Fig. 1. Figure 1(b) shows the x-y plane cross-section view of the metalens, where a metagrating
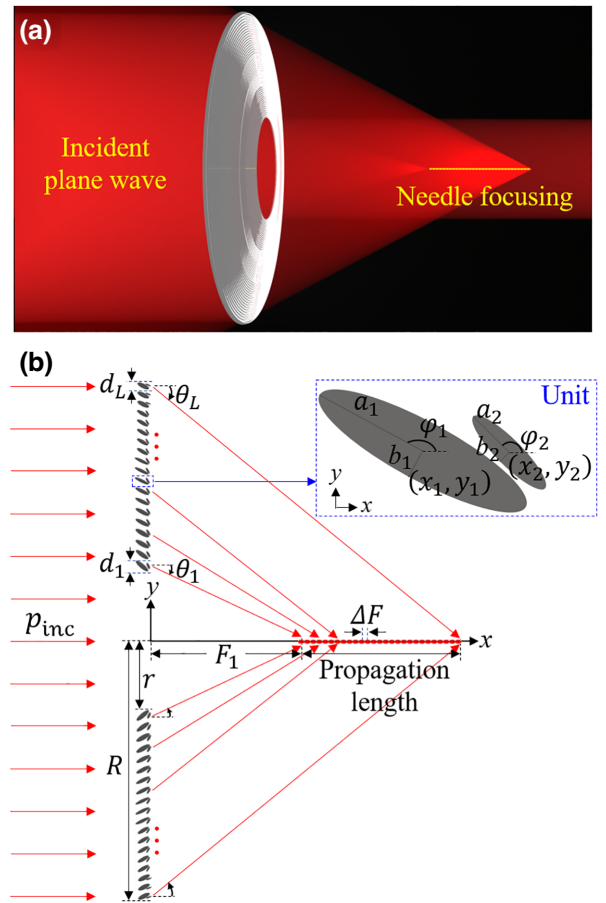

FIG. 1. The needle-focusing effect enabled by a metagrating-based metalens. (a) Schematic of the metalens and it needle-focusing effect. (b) A 2D cross section of the metalens, where the 3D lens can be obtained by rotating its 2D cross section around the x axis. A metagrating composed of 50 meta-atoms is surrounding the central axis, where each meta-atom contains two elliptical iron cylinders. The Lth ($L = 1, 2, \ldots, 50$) meta-atom is intelligently designed to deflect a normally incident plane wave (p_{inc}) along the diffraction angle θ_L towards the Lth focal spot on the x axis. Different meta-atoms focus the wave energy into different focal spots, as indicated by red arrows, with a distance 0.5λ between neighboring spots. In this way, all focal spots form a quasicontinuous needle pattern on the x axis.

consists of 50 meta-atoms (i.e., unit cells of the metagrating) is surrounding the lens' central axis, with the first meta-atom being closest to the central axis. Each meta-atom is composed of two elliptical iron cylinders, and the geometric parameters include the major semiaxes a_1 and a_2, minor semiaxes b_1 and b_2, rotation angles φ_1 and φ_2, and their center positions (x_1, y_1) and (x_2, y_2), as shown in the inset of Fig. 1(b). We note that although the design of the metalens is based on a diffraction analysis in 2D, it is easy to extend the analysis to 3D by simply rotating the meta-atoms around the x axis (i.e., the central axis of the metalens).

The metalens works for waterborne sound, so the background medium is water, with a mass density $\rho = 1000 \text{ kg/m}^3$ and sound velocity $c_0 = 1490$ m/s. For the solid iron cylinders, their mass density, longitudinal velocity, and transverse velocity are $\rho_1 = 7670 \text{ kg/m}^3$, $c_p = 6010$ m/s, and $c_s = 3230$ m/s, respectively. Each meta-atom is independently designed so that the Lth ($L = 1, 2, \ldots, 50$) meta-atom deflects a normally incident plane wave (p_{inc}) of wavelength λ along a specific direction (with diffraction angle θ_L) towards the Lth focal spot on the x axis. Different meta-atoms focus the wave energy into different focal spots. One by one, these focal spots form a quasicontinuous needle pattern on the x axis, with a mutual distance ΔF between neighboring focal spots. The length measured from the first focal point to the last one is called the propagation length of the needle focusing pattern.

To realize the needle focusing effect, we start with the grating diffraction theory. When a plane wave is normally incident on a grating, it will be reflected and transmitted into several diffraction orders along different directions, i.e.,

$$n\frac{2\pi}{d} = k_0 \sin\theta \quad \text{for the } n\text{th transmission order} \quad (1)$$

$$m\frac{2\pi}{d} = k_0 \sin\eta \quad \text{for the } m\text{th reflection order} \quad (2)$$

where $n(m) = 0, \pm1, \pm2, \ldots$ denotes the diffraction order, d is the periodicity of grating, $k_0 = 2\pi/\lambda$ is the wave number in water, and $\theta(\eta)$ represents the angle of transmission (reflection).

Let us take the metagrating on the $+y$ direction as an example to demonstrate the design paradigm. We design each meta-atom individually so that its $-$first-order transmitted wave ($n = -1$) be the sole dominating channel. That is to say, the wave scattered by the Lth meta-atom propagates *exclusively* along the $n = -1$ channel with a diffraction angle θ_L, as shown in Fig. 1(b). Here n is negative because the transmitted wave deflects towards the $-y$ direction.

Following Eq. (1), the periodicity d_L and diffraction angle θ_L of the Lth meta-atom should satisfy

$$d_L = -\lambda/\sin\theta_L, \quad (3)$$

where $\lambda = c_0/f_0$ is the wavelength of the incident wave in water at the working frequency f_0. Without loss of generality, we assume that the working frequency is 500 kHz, so that the corresponding wavelength is $\lambda = 2.98$ mm in water. The radial distance from the first meta-atom to the central axis is $r = 50\lambda$, as marked in Fig. 1(b), leaving an open central region of that is reserved as an efficient water-flow channel [55].

As shown schematically in Fig. 1(b), the $n = -1$ order transmitted wave of the Lth meta-atom converges to the

Lth focal spot with a focal length $F_L = F_1 + (L-1)\Delta F$, where F_1 is the focal length of the first meta-atom. The first meta-atom has a periodicity of $d_1 = 5.79$ mm and a diffraction angle $\theta_1 = -31°$. Then its focal length $F_1 = 84.83\lambda$ can be determined by the geometric relation $F_1 = (r + d_1/2)/\tan(|\theta_1|)$. In order to obtain a quasicontinuous needle focusing pattern along the x axis, the distance between neighboring focal spots is set as $\Delta F = 0.5\lambda$. Thus, the second meta-atom has a focal length of $F_2 = F_1 + 0.5\lambda$, and its radial distance to the x axis is $r + d_1 + d_2/2$. Consequently, its diffraction angle is $\theta_2 = -\tan^{-1}(r + d_1 + d_2/2)/F_2 = -31.79°$. In a successive way, the diffraction angle for the Lth meta-atom can be uniquely determined by

$$\tan(|\theta_L|) = \left(r + \sum_{i=1,\ldots,L-1} d_i + d_L/2 \right) / (F_1 + (L-1)\Delta F) \quad (4)$$

with the help of Eqs. (3) and (4), we can obtain the periodicities and diffraction angles of all meta-atoms. After the geometrical parameters in the 2D cross section are determined, we can rotate all meta-atoms around the x axis to obtain a 3D metalens.

As mentioned previously, when a plane wave (p_{inc}) is normally incident on a grating, it will be reflected and refracted along several discrete channels with $n(m) = 0, \pm1, \pm2, \ldots$. In this work, we aim to utilize the minus-first-order ($n = -1$) transmission channel of each meta-atom to realize the needle focusing effect. To this end, we let all high-order diffraction channels [i.e., $n(m) = \pm2, \pm3, \ldots$] be evanescent in the far-field region, and thus we need only to consider the 0th and $\pm$1st diffraction orders. In this way, each meta-atom could have a geometrical structure as simple as possible, which can not only substantially reduce the difficulty of the inverse design process, but also is beneficial to the fabrication and testing of the metalens. According to Bragg's diffraction condition, the diffraction order of $|n(m)| = 2$ happens to be an evanescent wave when the diffraction angle $|\theta_L|$ takes the critical value of $30°$. Thus, as long as $|\theta_L| > 30°$, only $n = 0, \pm1$ and $m = 0, \pm1$ are the propagating orders.

Along this line, we let $|\theta_L|$ of all meta-atoms be larger than $30°$. This is the reason why we choose $\theta_1 = -31°$ for the first meta-atom. As shown in Fig. 1, other meta-atoms ($L = 2, 3, \ldots$) have their diffraction angles $|\theta_L| > |\theta_1|$, which means that for every meta-atom in the lens, we need only to manipulate six diffraction channels, including three reflection channels ($m = 0, \pm1$) and three transmission channels ($n = 0, \pm1$). In particular, we design each meta-atom intelligently to control its six diffraction orders so that the desired focusing functionality is implemented *exclusively* by the $-$first transmission channel ($n = -1$),

TABLE I. Optimized geometric parameters of the meta-atoms.

No.	L	a_1/mm	b_1/mm	φ_1/rad	(x_1, y_1)/mm	a_2/mm	b_2/mm	φ_2/rad	(x_2, y_2)/mm
1	1	3.89	1.15	2.440	$(-3.42, 2.78)$	1.68	0.62	1.982	$(-0.32, 2.80)$
2	2	3.72	1.13	2.526	$(-3.38, 2.75)$	1.70	0.60	2.058	$(-0.31, 2.92)$
3	3,4	3.81	1.18	2.623	$(-3.28, 2.40)$	1.72	0.61	2.083	$(-0.31, 2.65)$
4	5,6	3.77	1.04	2.657	$(-3.25, 2.22)$	1.68	0.57	2.109	$(-0.32, 2.47)$
5	7,8	3.76	0.95	2.679	$(-3.36, 2.26)$	1.62	0.53	2.120	$(-0.45, 2.49)$
6	9–11	3.78	0.82	2.688	$(-3.56, 2.34)$	1.63	0.53	2.116	$(-0.61, 2.51)$
7	12–16	3.13	0.96	2.614	$(-3.17, 2.24)$	1.51	0.46	2.109	$(-0.78, 2.51)$
8	17–23	3.16	1.13	2.675	$(-2.83, 2.28)$	1.44	0.38	2.750	$(-0.44, 2.79)$
9	24–32	3.19	0.94	2.644	$(-3.28, 2.17)$	1.35	0.33	2.583	$(-1.01, 2.43)$
10	33–50	3.19	0.80	2.644	$(-3.24, 2.00)$	1.38	0.35	2.352	$(-0.89, 1.96)$
11	51–79	3.21	0.69	2.641	$(-3.12, 1.67)$	1.40	0.35	2.363	$(-0.85, 1.60)$
12	80–116	3.20	0.63	2.642	$(-3.11, 1.85)$	1.56	0.39	2.338	$(-0.78, 1.79)$
13	117–149	3.20	0.57	2.667	$(-3.20, 1.72)$	1.54	0.39	2.290	$(-0.81, 1.72)$
14	150–180	3.20	0.57	2.716	$(-3.24, 1.68)$	1.50	0.41	2.193	$(-0.71, 1.87)$

and at the same time the other five propagating channels ($m = 0, \pm 1$ and $n = 0, +1$) are completed depressed. In contrast, if we choose a smaller diffraction angle with $|\theta_L| < 30°$, we will have to simultaneously manipulate at least ten diffraction orders ($n, m = 0, \pm 1, \pm 2$) to realize the focusing effect, which poses a more difficult inverse design task and inevitably requires a more complicated configuration of the meta-atom.

When the incident plane wave is scattered by the meta-atom made of iron, both longitudinal and transverse elastic wave modes in iron cylinders need to be considered, which not only raises a much more complicated scattering problem than the scalar one (such as the electromagnetic or acoustic wave scattering problem), but also brings richer physics. For example, the multiple-scattering effects [57, 58] of sound waves between any two solid cylinders need to be taken into consideration. To resolve this challenge, we use an intelligent optimization method based on particle swarm optimization (PSO). PSO is an evolutionary optimization technique that solves a problem by having a population of candidate solutions (i.e., particles) flowing around in the search space according to a simple mathematical formula over the particle's position and velocity, and it can search for candidate solutions in very large spaces. In applying the PSO algorithm, we take the geometrical parameters of each meta-atom, i.e., (a_1, a_2, b_1, b_2, φ_1, φ_2, x_1, x_2, y_1, and y_2) of the two elliptic cylinders, as the optimization variables. Our optimization objective is to ensure that the diffracted wave propagates exclusively along the $n = -1$ transmission channel (i.e., $T_{-1} \rightarrow 100\%$), and all other propagating diffraction channels are completely depressed, (i.e., $T_{0,+1} \rightarrow 0$ and $R_{0,\pm 1} \rightarrow 0$). With the help of the PSO algorithm, the optimized geometric parameters of all 50 meta-atoms can be quickly obtained, which are listed in Table I.

Each row in Table I represents a set of optimized geometric parameters for the meta-atoms, and a total of ten

sets of parameters are needed to construct a metalens consisting of 50 meta-atoms. For example, the first and second rows of Table I show the sets of parameters for the first and second meta-atoms, respectively, with corresponding diffraction angle $\theta_1 = -31°$ and $\theta_2 = -31.79°$. From the third row of Table I, however, the diffraction angle θ_L becomes relatively large, so that two or more neighboring meta-atoms can share the same set of optimized parameters. For example, the seventh and eighth meta-atoms (i.e., $L = 7, 8$) share the same set of parameters (as listed in the fifth row of Table I), and their diffraction angles have a minor difference, with $\theta_7 = -35.19°$ and $\theta_8 = -35.78°$. In this way, for the metalens consisting of 50 meta-atoms, we need only ten sets of distinct geometrical parameters to achieve the needle focusing functionality, which not only simplifies the design process but also reduces the fabrication and testing cost.

To verify the optimization results of PSO, we use the pressure acoustics and solid mechanics module of the acoustic-solid interaction interface in COMSOL Multiphysics for the full-wave numerical simulations, where both longitudinal and transverse wave modes in iron cylinders are rigorously taken into consideration. We firstly independently design each meta-atom to manipulate the diffracted wave along the desired direction, with the simulation setup shown in Fig. 2(a). The upper and lower boundaries of the simulation domain are set as periodic boundary conditions (PBCs), with a plane wave incident from the left-hand side. Perfectly matched layers (PMLs) are applied on the left and right boundaries to absorb the outgoing scattered waves. The two orange solid lines are the integration boundaries, where the transmittance is evaluated.

Let us take the first and 50th meta-atoms as an example to demonstrate their intriguing wave-deflection ability. In Fig. 2(b), we plot both acoustic pressure field in water and stress field (i.e., the first Cauchy stress invariant) in iron
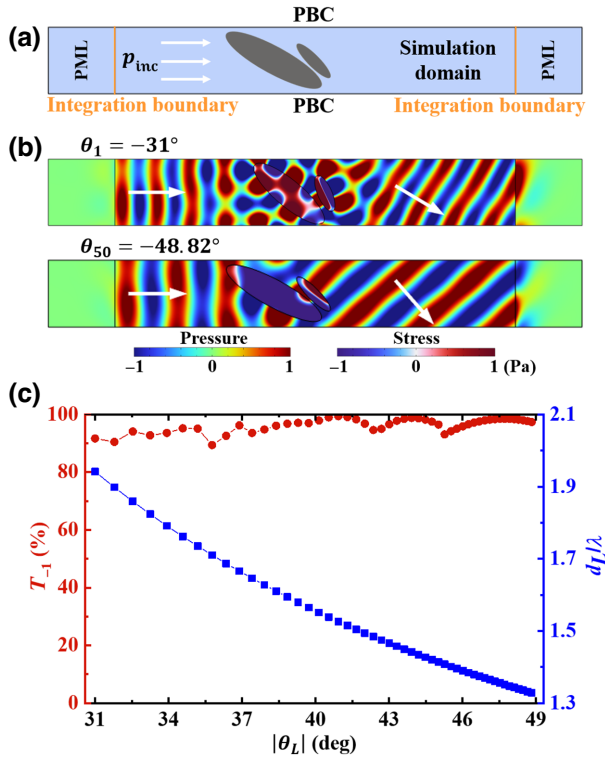
FIG. 2. Design of each meta-atom. (a) Numerical simulation setup in COMSOL Multiphysics. (b) Shows the wave deflection abilities of the first and 50th meta-atoms, respectively. White arrows represent the directions of incident and transmitted waves. Strong coupling between the incident acoustic wave and the elastic vibration modes in solid cylinders can be seen. (c) The $n = -1$ channel transmission efficiency T_{-1} and periodicity d_L of the Lth meta-atom as a function of the refraction angle $|\theta_L|$.
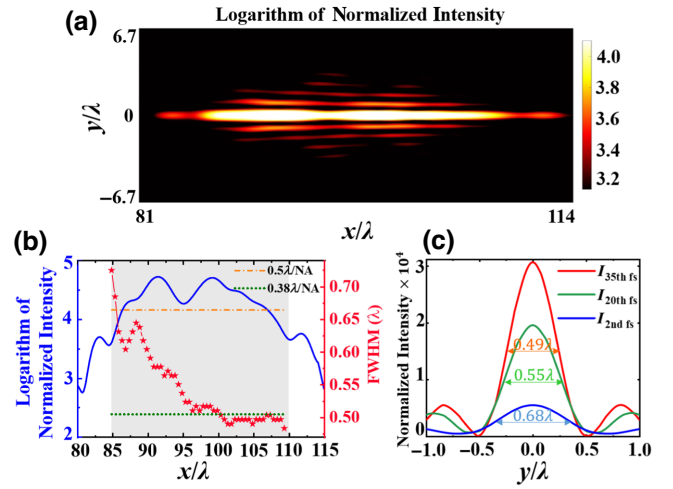

FIG. 3. The acoustic needle-focusing effect for a metalens consisting of 50 meta-atoms. (a) Shows the logarithm of normalized pressure intensity ($\log_{10}I_{\mathrm{norm}}$) within the x-y plane, where a needle pattern with a propagation length approximately 25λ can be seen. (b) Shows the logarithm of pressure-intensity profile along the x axis (blue line) and the transverse FWHM of each focal spot (red stars). Orange dot-dashed line and green dotted line represent the Rayleigh-Abbe diffraction limit ($0.5\lambda/\mathrm{NA} = 0.664\lambda$) and superoscillation criterion ($0.38\lambda/\mathrm{NA} = 0.505\lambda$), respectively. (c) Shows the pressure-intensity profiles along the y axis for the second, 20th, and 35th focal spots, respectively, with the corresponding FWHMs explicitly marked.

cylinders for the meta-atoms. The subwavelength features of the stress field in solid cylinders and the distributions of pressure and stress fields across the cylinder's boundary show strong coupling between the incident acoustic wave in water and the elastic vibration modes in solid material. It is this coupling that enables the anomalous transmission along the $n = -1$ channel. The corresponding transmission efficiencies T_{-1} are found to be 91.7% and 97.4%, respectively, for the first and 50th meta-atoms. In Fig. 2(c) we plot the transmission efficiencies T_{-1} for all 50 meta-atoms, and they all exhibit high values close to 100%. We note that such a high transmittance can be also achieved with acoustic metamaterials or metasurfaces [59,60], where a broadband and wide-angle impedance matching was demonstrated.

III. RESULTS

In this section, we demonstrate the needle-focusing effect of the metalens. We begin with the metalens composed of 50 meta-atoms. The outmost meta-atom, i.e., the 50th meta-atom, has a diffraction angle of $\theta_{50} = -48.82°$.

Therefore, the metalens has a numerical aperture of $\mathrm{NA} = \sin(|\theta_{50}|) = 0.753$. The ring-shaped metalens has an outer radius $R = 125.66\lambda$ and an inner radius $r = 50\lambda$, which means that the open central region occupies a big area ratio of $\sigma = r^2/R^2 \approx 15.8\%$. Such a planar and hollow-center configuration of the metalens is not only advantageous for its integration with other planar components to develop comprehensive and multifunctional devices, but also reserves an efficient channel for a free water flow that is needed in various underwater applications [55,56].

When a plane wave of $p_{\mathrm{inc}} = 1[Pa]e^{ikx}\hat{x}$ is incident on the metalens, the resultant focusing effect is shown in Fig. 3. We plot the logarithm of the normalized pressure intensity $\log_{10}I_{\mathrm{norm}}$ in the x-y plane in Fig. 3(a), where the pressure intensity I_{meta} is normalized by the intensity of the incident wave I_0, i.e., $I_{\mathrm{norm}} = I_{meta}/I_0$. The needle-focusing effect is clearly observed. Our design target is to realize a long needle pattern starting from $F_1 = 84.83\lambda$ until $F_{50} = F_1 + (50 - 1)\Delta F = 109.33\lambda$, with a propagation length approximately 25λ. We plot the logarithm of the pressure-intensity profile along the x axis by a blue line in Fig. 3(b), where the needle-focusing region is highlighted by a gray background (starting from $y \approx 85\lambda$ to 110λ), agreeing very well with the initial design target.

In Fig. 3(b) we also show the FWHM in the transverse plane for all focal spots by red stars, where a high-resolution focusing character can be identified. It is well known that the resolution of conventional optical or acoustic devices is limited by the Rayleigh-Abbe diffraction limit of $0.5\lambda/\text{NA}$, implying that the FWHM of conventional focusing devices is usually larger than $0.5\lambda/\text{NA}$. If, however, the FWHM is less than this limit, it is called a subdiffraction focusing. We mark the Rayleigh-Abbe diffraction limit as an orange dash-dot line in Fig. 3(b), and it can be seen that the FWHM always stays below the Rayleigh-Abbe limit in the needle-focusing region and exhibits a subdiffractive character.

The above subdiffraction focusing effect is due to the fact that a band-limited function in the focus plane could oscillate faster than the highest transverse Fourier components ($k_{||,\text{max}}$) it contains, a phenomenon called superoscillation in the literature [4–6]. In fact, there were recently growing interests in the study of far-field superresolution devices that break the Rayleigh-Abbe diffraction limit. In this work, the subdiffraction focusing of waterborne acoustic wave is attained in the far-field region with a very large focal length, i.e., $85\lambda < F < 110\lambda$. For such a long distance, all higher-order ($|n| \geq 2$) transmission channels have quickly decayed to zero because they are evanescent modes and cannot propagate to the far-field region. Thus, the subdiffraction focusing effect comes only from the propagating modes, i.e., the $|n| \leq 1$ transmission channels. According to the design principle of the metalens, it is the far-field coherent interference of the $n = -1$ transmission channel that results in the subdiffraction focusing phenomenon, and the underneath physical mechanism can be ascribed to the superoscillation effect [4–6].

In Fig. 3(b) we have plotted a dotted green line to mark the superoscillation criterion ($0.38\lambda/\text{NA}$), below which is the superoscillation regime [4–6]. Accordingly, in Fig. 3(c) we plot the pressure-intensity profiles along the transverse y direction through three focal spots at $F_2 = F_1 + \Delta F = 85.33\lambda$, $F_{20} = F_1 + 19\Delta F = 94.33\lambda$, and $F_{35} = F_1 + 34\Delta F = 101.33\lambda$, respectively. These focal spots are induced by waves scattered by the second, 20th, and 35th meta-atoms, respectively. As shown clearly in Fig. 3(c), as their intensity peaks become higher and narrower, the corresponding FWHMs become smaller, with $\text{FWHM}_{2\text{nd}} > \text{FWHM}_{20\text{th}} > \text{FWHM}_{35\text{th}}$. In fact, for the 35th focal spot, the corresponding $\text{FWHM}_{35\text{th}} = 0.49\lambda < 0.5\lambda/\text{NA}$, residing in the superoscillation regime.

In the following, we aim to further improve the needle-focusing performance through constructing three diameter-extended metalenses by adding more meta-atoms to the peripheral region of the previous metalens studied in Fig. 3. In this way, we can achieve the needle-focusing patterns with longer propagation lengths. In particular, in Fig. 4 we show the focusing effects with three larger metalenses consisting of 80, 90, and 180 meta-atoms,
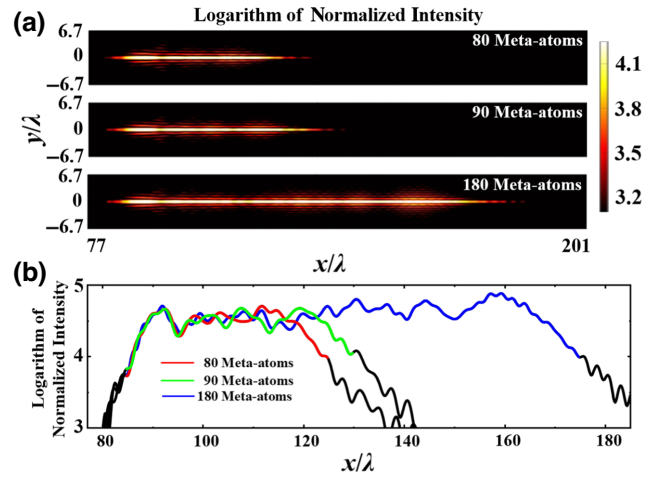

FIG. 4. The needle-focusing patterns with three larger metalenses consisting of 80, 90, and 180 meta-atoms, respectively. (a) Shows the logarithm of normalized pressure intensity within the x-y plane, where the propagation lengths of 40λ, 45λ, and 90λ can be observed, respectively. (b) Shows the logarithm of pressure-intensity profile along the x axis for three metalenses, where the colored parts of the intensity curves show the high-intensity focusing regions predicted by the initial design targets.

respectively, with the geometrical parameters of the added meta-atoms listed in the last four rows of Table I. The propagation lengths of them are 40λ, 45λ, and 90λ, respectively. Figure 4(a) shows the logarithm of the normalized pressure intensity in the x-y plane, where the high-intensity focusing patterns are observed for all three lenses. Meanwhile, the initial design targets of high-intensity profiles along the x axis are plotted as red, green, and blue curves, respectively, in Fig. 4(b), and all of them agreeing very well with the actual results. As the increase of the number of meta-atoms, both the propagation length and maximum intensity of the focal spots increase. Noticeably, the largest metalens consisting of 180 meta-atoms exhibits a propagation length of 90λ with the needle pattern starting from $F_1 = 84.83\lambda$, and the maximum intensity reaches a very high value of 7.6×10^4, implying a huge energy concentration effect. In principle, a longer and stronger needle-focusing pattern can be achieved when more meta-atoms are appended to the existing metalens.

Interestingly, while neither wideband nor multifrequency performances were considered during the optimization, we find that the metagrating-based metalens can work effectively at different frequencies around the design frequency f_0. Taking the largest metalens composed of 180 meta-atoms as an example, the logarithm of normalized pressure-intensity profiles along the x axis are plotted in Fig. 5(a) at frequencies $0.95f_0$, f_0, and $1.05f_0$, respectively. Although the metalens exhibits the best focusing performance at f_0, it still keeps a satisfying focusing functionality
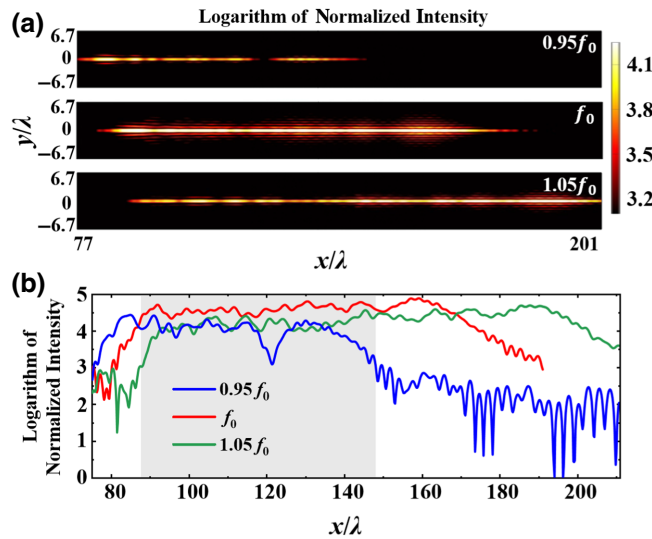
FIG. 5. The focusing performance at different frequencies. (a) Shows the logarithm of normalized pressure intensity within the x-y plane at frequencies $0.95f_0$, f_0, and $1.05f_0$, respectively. (b) Shows the logarithm of pressure-intensity profiles along the x axis at $0.95f_0$, f_0, and $1.05f_0$, where the gray background marks the overlapped needle focusing region valid for a continuum of frequency, i.e., $0.95f_0 < f < 1.05f_0$.

at both lower and higher frequencies. In particular, the foci of different frequencies partially overlap with each other, creating a shared focusing zone located in the far-field region with a long distance (87λ) from the metalens. This overlapped focusing zone has a significant length of 61λ, as marked by the gray background in Fig. 5(b), where a continuous range of frequency (i.e., $0.95f_0 < f < 1.05f_0$) can be focused simultaneously. In this way, we realize an achromatic focusing of acoustic waves. We expect that such a far-field, achromatic, high-intensity, and super-oscillatory needle-focusing effect may find applications in ultrasonic imaging and underwater communications.

IV. DISCUSSION

In the design process of optimizing the geometry of each meta-atom and assembling them into a metalens, we cautiously and deliberately keep neighboring meta-atoms having almost the same configurations. Figure 6 shows the configurations of the first–fifth meta-atoms in the metalens, and we can observe that there is only minor difference in the geometrical parameters between neighboring meta-atoms. With such a slowly and adiabatically varying of geometry, the coupling between neighboring meta-atoms are taken into consideration to a good approximation by the PBCs, as specified in Fig. 2. Thus, it is not necessary here to optimize or adjust each meta-atom's parameters again when assembling them into a metalens.
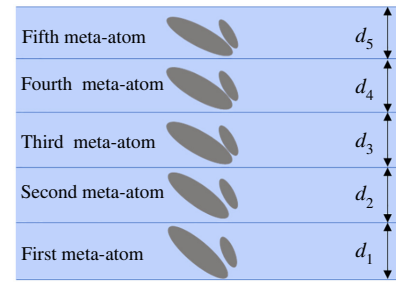

FIG. 6. The configurations of the first–fifth meta-atoms in the metalens.

In some situations, however, we can choose to optimize once again all parameters of the metalens to realize an extreme focusing performance. For example, we can try to suppress or even eliminate the side needles in Fig. 3 by manipulating the phase of the acoustic field along the needle pattern (details of the phase control method can be found in Appendix A). But such further studies are out of the scope of the current work, because in this paper we aim to propose the design paradigm of a metalens to realize an achromatic needle-focusing function with superresolution.

Furthermore, we note that it is also possible to realize a needle-focusing function with a phase-modulating metasurface. It is well known that a metasurface-based metalens is usually designed according to the required gradient phase profile, $\phi(y) = (2\pi/\lambda)\left(\sqrt{y^2 + F^2} - F\right)$ at position y on the metasurface, to achieve the focusing effect, with F being the focal length. Then the continuous phase profile $\phi(y)$ is discretized with a number of unit cells, each providing a phase shift $\phi(y_i)$ sampled on this continuous phase profile. In this way, the diffracted waves by all unit cells of the metasurface can arrive at the focal point with the same phase, leading to a constructive interference and the focusing functionality.

In a similar way, another phase profile $\phi(y)$ can be discretized and implemented on the metasurface so that

$$\phi(y_1) = \frac{2\pi}{\lambda}\left(\sqrt{y_1^2 + F_1^2} - F_1\right),$$

$$\phi(y_2) = \frac{2\pi}{\lambda}\left(\sqrt{y_2^2 + F_2^2} - F_2\right),$$

$$\phi(y_3) = \frac{2\pi}{\lambda}\left(\sqrt{y_3^2 + F_3^2} - F_3\right),$$

and so on, with y_i denoting different positions of the unit cells on the metasurface. When a small distance $\Delta F = F_{i+1} - F_i$ between neighboring focal spots are implemented, all focal spots of the metasurface can form a quasicontinuous needle pattern on the lens' axis.

Since the metasurface is based on the GSL instead of the grating diffraction theory, the diffraction efficiency

of a metasurface may be substantially lower than that of metagrating at large steering angles, due to the mismatched wave impedance. Therefore, the overall focusing efficiency of a metasurface-based lens is not expected as high as that of a metagrating-based lens.

V. CONCLUSIONS

To conclude, we propose a metagrating-based metalens to realize a far-field subdiffraction needle-focusing effect for waterborne sound. The metalens is open in the central region, and has a grating of meta-atoms in the peripheral region. Each meta-atom contains two elliptical iron cylinders in the radial cross section, which are independently and intelligently designed to reroute the normally impinging plane wave along specified direction towards the focal spot. Different meta-atoms focus the wave energy into different focal spots, which are intendedly design to form a continuous needle pattern in the far-field region with high efficiency. Interestingly, the conventional Rayleigh-Abbe diffraction limit is broken due to the coherent interference of the diffraction channels. Furthermore, since no sharp resonance is utilized, the needle-focusing functionality can be attained over a continuous range of frequency, realizing an achromatic focusing effect. The planar and simple configuration of the metalens, as well as its achromatic and superoscillatory focusing functionality, may find applications such as medical diagnosing and treating, and underwater communication and navigation.

ACKNOWLEDGMENTS

APPENDIX A: PHASE CONTROL OF THE ACOUSTIC FIELD ALONG THE NEEDLE PATTERN

In this Appendix, we will show that, in principle, we can control the phase of the acoustic field along the needle pattern. For a plane wave impinging on the metalens, all meta-atoms have the same initial phase because they lie in the same planar wave front. But their phase could be different after passing through the meta-atoms, bending toward and finally arriving at the focal spots. In this diffraction process, the total phase change ϕ_f of each wave beam diffracted by the meta-atom is composed of two parts. The first part is the transmission phase ϕ_t, accompanying the transmission of the wave beam through the meta-atom. The second part is the propagation phase ϕ_p, accumulated along the propagation path from each meta-atom to the corresponding focal spot.

Obviously, the second part ϕ_p is determined by the geometrical parameters shown in Fig. 1. Once the diffraction

angle θ_L and periodicity d_L of each meta-atom are determined, the propagation phase ϕ_p is fixed and cannot be changed. But the transmission phase ϕ_t can be tuned. As long as we can control ϕ_t in such a way that the total phase change ($\phi_f = \phi_t + \phi_p$) is kept the same for all meta-atoms, we can realize the target that all wave beams arriving at the needle pattern with the same phase.

———

[1] W. T. Chen, A. Y. Zhu, V. Sanjeev, M. Khorasaninejad, Z. Shi, E. Lee, and F. Capasso, A broadband achromatic metalens for focusing and imaging in the visible, Nat. Nanotechnol. **13**, 220 (2018).

[2] S. Wang, P. C. Wu, V. C. Su, Y. C. Lai, M. K. Chen, H. Y. Kuo, B. H. Chen, Y. H. Chen, T. T. Huang, J. H. Wang, R. M. Lin, C. H. Kuan, T. Li, Z. Wang, S. Zhu, and D. P. Tsai, A broadband achromatic metalens in the visible, Nat. Nanotechnol. **13**, 227 (2018).

[3] M. V. Berry and S. Popescu, Evolution of quantum super-oscillations and optical superresolution without evanescent waves, J. Phys. A: Math. Gen. **39**, 6965 (2006).

[4] G. Chen, Z. Q. Wen, and C. W. Qiu, Superoscillation: From physics to optical applications, Light: Sci. Appl. **8**, 56 (2019).

[5] N. I. Zheludev and G. Yuan, Optical superoscillation technologies beyond the diffraction limit, Nat. Rev. Phys. **4**, 16 (2022).

[6] G. Gbur, Using superoscillations for superresolved imaging and subwavelength focusing, Nanophotonics **8**, 205 (2019).

[7] F. M. Huang, Y. Chen, F. J. G. de Abajo, and N. I. Zheludev, Optical super-resolution through super-oscillations, J. Opt. A: Pure Appl. Opt. **9**, S285 (2007).

[8] E. T. F. Rogers, J. Lindberg, T. Roy, S. Savo, J. E. Chad, M. R. Dennis, and N. I. Zheludev. Nat. Mater. **11**, 432 (2012).

[9] K. Huang, H. Ye, J. Teng, S. P. Yeo, B. Luk'yanchuk, and C. W. Qiu, Optimization-free superoscillatory lens using phase and amplitude masks, Laser Photonics Rev. **8**, 152 (2014).

[10] G. H. Yuan, E. T. Rogers, and N. I. Zheludev, Achromatic super-oscillatory lenses with sub-wavelength focusing, Light: Sci. Appl. **6**, e17036 (2017).

[11] F. Zhao, Z. Li, X. Dai, X. Liao, S. Li, J. Cao, Z. Shang, Z. Zhang, G. Liang, G. Chen, H. Li, and Z. Wen, Broadband achromatic sub-diffraction focusing by an amplitude-modulated terahertz metalens, Adv. Opt. Mater. **8**, 2000842 (2020).

[12] H. S. Hsu, F. Zheng, Y. Li, C. Lee, Q. Zhou, and K. Kirk Shung, Focused high frequency needle transducer for ultrasonic imaging and trapping, Appl. Phys. Lett. **101**, 024105 (2012).

[13] J. Zhao, H. Ye, K. Huang, Z. N. Chen, B. Li, and C. W. Qiu, Manipulation of acoustic focusing with an active and configurable planar metasurface transducer, Sci. Rep. **4**, 6257 (2014).

[14] X. D. Fan, Y. F. Zhu, B. Liang, J. Yang, and J. C. Cheng, Broadband convergence of acoustic energy with binary reflected phases on planar surface, Appl. Phys. Lett. **109**, 243501 (2016).

[15] C. Fei, Y. Li, B. Zhu, C. T. Chiu, Z. Chen, D. Li, Y. Yang, K. Kirk Shung, and Q. Zhou, Contactless microparticle control

via ultrahigh frequency needle type single beam acoustic tweezers, Appl. Phys. Lett. **109,** 173509 (2016).

[16] Y. X. Shen, Y. G. Peng, F. Cai, K. Huang, D. G. Zhao, C. W. Qiu, H. Zheng, and X. F. Zhu, Ultrasonic super-oscillation wave-packets with an acoustic meta-lens, Nat. Commun. **10,** 3411 (2019).

[17] D. C. Chen, Q. Wei, L. L. Huang, X. F. Zhu, and D. J. Wu, Acoustic needle focusing induced by metasurface-generated accelerating beams, Europhys. Lett. **129,** 48001 (2020).

[18] Q. Liu, K. Chen, J. Hu, and T. Morita, An ultrasonic tweezer with multiple manipulation functions based on the double-parabolic-reflector wave-guided high-power ultrasonic transducer, IEEE Trans. Ultrason. Ferroelectr. Freq. Control **67,** 2471 (2020).

[19] J. He, X. Jiang, H. Zhao, C. Zhang, Y. Zheng, C. Liu, and D. Ta, Broadband three-dimensional focusing for an ultrasound scalpel at megahertz frequencies, Phys. Rev. Appl. **16,** 024006 (2021).

[20] S. Hur, H. Choi, G. H. Yoon, N. W. Kim, D. G. Lee, and Y. T. Kim, Planar ultrasonic transducer based on a metasurface piezoelectric ring array for subwavelength acoustic focusing in water, Sci. Rep. **12,** 1485 (2022).

[21] J. Ma, J. Zhao, H. Chen, L. P. Sun, J. Li, and B. O. Guan, Transparent microfiber Fabry-Perot ultrasound sensor with needle-shaped focus for multiscale photoacoustic imaging, Photoacoustics **30,** 100482 (2023).

[22] Y. Ra'di, D. L. Sounas, and A. Alù, Metagratings: Beyond the limits of graded metasurfaces for wave front control, Phys. Rev. Lett. **119,** 067404 (2017).

[23] A. Epstein and O. Rabinovich, Unveiling the properties of metagratings via a detailed analytical model for synthesis and analysis, Phys. Rev. Appl. **8,** 054037 (2017).

[24] N. Yu, P. Genevet, M. A. Kats, F. Aieta, J. Tetienne, F. Capasso, and Z. Gaburro, Light propagation with phase discontinuities: Generalized laws of reflection and refraction, Science **334,** 333 (2011).

[25] A. Díaz-Rubio and S. A. Tretyakov, Acoustic metasurfaces for scattering-free anomalous reflection and refraction, Phys. Rev. B **96,** 125409 (2017).

[26] B. Assouar, B. Liang, Y. Wu, Y. Li, J. C. Cheng, and Y. Jing, Acoustic metasurfaces, Nat. Rev. Mater. **3,** 460 (2018).

[27] J. Mei, G. Ma, M. Yang, Z. Yang, W. Wen, and P. Sheng, Dark acoustic metamaterials as super absorbers for low-frequency sound, Nat. Commun. **3,** 756 (2012).

[28] Y. Li, B. Liang, X.-Y. Zou, and J. C. Cheng, Extraordinary acoustic transmission through ultrathin acoustic metamaterials by coiling up space, Appl. Phys. Lett. **103,** 063509 (2013).

[29] J. Zhao, B. Li, Z. N. Chen, and C. W. Qiu, Redirection of sound waves using acoustic metasurface, Appl. Phys. Lett. **103,** 151604 (2013).

[30] G. Ma, M. Yang, S. Xiao, Z. Yang, and P. Sheng, Acoustic metasurface with hybrid resonances, Nat. Mater. **13,** 873 (2014).

[31] J. Mei and Y. Wu, Controllable transmission and total reflection through an impedance-matched acoustic metasurface, New J. Phys. **16,** 123007 (2014).

[32] Y. Cheng, C. Zhou, B. G. Yuan, D. J. Wu, Q. Wei, and X. J. Liu, Ultra-sparse metasurface for high reflection of

low-frequency sound based on artificial Mie resonances, Nat. Mater. **14,** 1013 (2015).

[33] Y. Li and B. M. Assouar, Acoustic metasurface-based perfect absorber with deep subwavelength thickness, Appl. Phys. Lett. **108,** 063502 (2016).

[34] J. Li, C. Shen, A. Díaz-Rubio, S. A. Tretyakov, and S. A. Cummer, Systematic design and experimental demonstration of bianisotropic metasurfaces for scattering-free manipulation of acoustic wavefronts, Nat. Commun. **9,** 1342 (2018).

[35] J. Mei, X. Zhang, and Y. Wu, Ultrathin metasurface with high absorptance for waterborne sound, J. Appl. Phys. **123,** 091710 (2018).

[36] X. Jiang, Y. Li, D. Ta, and W. Wang, Ultrasonic sharp autofocusing with acoustic metasurface, Phys. Rev. B **102,** 064308 (2020).

[37] H. T. Zhou, W. X. Fu, Y. F. Wang, and Y. S. Wang, High-efficiency ultrathin nonlocal waterborne acoustic metasurface, Phys. Rev. Appl. **15,** 044046 (2021).

[38] D. Torrent, Acoustic anomalous reflectors based on diffraction grating engineering, Phys. Rev. B **98,** 060101 (2018).

[39] Y. Fu, C. Shen, Y. Cao, L. Gao, H. Chen, C. T. Chan, S. A. Cummer, and Y. Xu, Reversal of transmission and reflection based on acoustic metagratings with integer parity design, Nat. Commun. **10,** 2326 (2019).

[40] Y. Yang, H. Jia, Y. Bi, H. Zhao, and J. Yang, Experimental demonstration of an acoustic asymmetric diffraction grating based on passive parity-time-symmetric medium, Phys. Rev. Appl. **12,** 034040 (2019).

[41] L. Fan and J. Mei, Metagratings for waterborne sound: Various functionalities enabled by an efficient inverse design approach, Phys. Rev. Appl. **14,** 044003 (2020).

[42] Y. K. Chiang, S. Oberst, A. Melnikov, L. Quan, S. Marburg, A. Alù, and D. A. Powell, Reconfigurable acoustic metagrating for high-efficiency anomalous reflection, Phys. Rev. Appl. **13,** 064067 (2020).

[43] Z. Du and J. Mei, Metagrating-based acoustic wavelength division multiplexing enabled by deterministic and probabilistic deep learning models, Phys. Rev. Res. **4,** 033165 (2022).

[44] J. He, X. Jiang, D. Ta, and W. Wang, Experimental demonstration of underwater ultrasound cloaking based on metagrating, Appl. Phys. Lett. **117,** 091901 (2020).

[45] Y. Fu, C. Shen, X. Zhu, J. Li, Y. Liu, S. Cummer, and Y. Xu, Sound vortex diffraction via topological charge in phase gradient metagratings, Sci. Adv. **6,** eaba9876 (2020).

[46] L. Fan and J. Mei, Acoustic metagrating circulators: Non-reciprocal, robust, and tunable manipulation with unitary efficiency, Phys. Rev. Appl. **15,** 064002 (2021).

[47] L. Fan and J. Mei, Multifunctional waterborne acoustic metagratings: From extraordinary transmission to total and abnormal reflection, Phys. Rev. Appl. **16,** 044029 (2021).

[48] J. Mei, L. Fan, and X. Hong, Elastic metagratings with simultaneously highly efficient control over longitudinal and transverse waves for multiple functionalities, Phys. Rev. Appl. **18,** 014002 (2022).

[49] J. Mei, L. Fan, and X. Hong, Elastic metagratings with simultaneous modulation of reflected and transmitted waves, Crystals **12,** 901 (2022).

[50] J. Qian, J. P. Xia, H. X. Sun, Y. Wang, Y. Ge, S. Q. Yuan, Y. Yang, X. J. Liu, and B. Zhang, Aperiodic metagratings for high-performance multifunctional acoustic lenses, Adv. Mater. Technol. **5,** 2000542 (2020).

[51] M. Kang, Y. Ra'di, D. Farfan, and A. Alù, Efficient focusing with large numerical aperture using a hybrid metalens, Phys. Rev. Appl. **13,** 044016 (2020).

[52] Y. K. Chiang, L. Quan, Y. Peng, S. Sepehrirahnama, S. Oberst, A. Alù, and D. A. Powell, Scalable metagrating for efficient ultrasonic focusing, Phys. Rev. Appl. **16,** 064014 (2021).

[53] J. Mei, L. Fan, and X. B. Hong, Broadband and high-numerical-aperture sharp focusing for waterborne sound with metagrating-based lens, New J. Phys. **24,** 093014 (2022).

[54] Y. J. Lu, H. Y. Zou, J. Qian, Y. Wang, Y. Ge, S. Q. Yuan, H. X. Sun, and X. J. Liu, Multifunctional reflected lenses based on aperiodic acoustic metagratings, Appl. Phys. Lett. **119,** 173501 (2021).

[55] L. Fan and J. Mei, Flow-permeable and tunable metalens for subdiffraction waterborne-sound focusing, Phys. Rev. Appl. **19,** 024026 (2023).

[56] J. Mei, L. Fan, and X. Hong, Acoustic metalens with switchable and sharp focusing, Appl. Phys. Express **16,** 077002 (2023).

[57] J. Mei, Z. Liu, W. Wen, and P. Sheng, Effective mass density of fluid-solid composites, Phys. Rev. Lett. **96,** 024301 (2006).

[58] J. Mei, Z. Liu, J. Shi, and D. Tian, Theory for elastic wave scattering by a two-dimensional periodical array of cylinders: An ideal approach for band-structure calculations, Phys. Rev. B **67,** 245107 (2003).

[59] C. Liu, J. Luo, X. Liu, and Y. Lai, Hydroacoustic high absorption with broadband and wide-angle impedance matching, Phys. Rev. Appl. **18,** 044008 (2022).

[60] J. Shi, C. Liu, C. Guo, H. Chu, X. Liu, J. Christensen, and Y. Lai, Broadband acoustic metaveils for configurable camouflage, Phys. Rev. Appl. **18,** 064064 (2022).